Towards Visual Proteomics at High Resolution

Felix J. B. Bäuerlein [1,2,3]* and **Wolfgang Baumeister** [1]*

1 - **Max-Planck-Institute of Biochemistry,** Department for Molecular Structural Biology, Am Klopferspitz 18, 82152 Planegg, Germany
2 - **Georg-August-University,** Institute for Neuropathology, Robert-Koch-Strasse 40, 37075 Göttingen, Germany
3 - **Cluster of Excellence** "**Multiscale Bioimaging: from Molecular Machines to Networks of Excitable Cells**" **(MBExC),** University of Göttingen, Germany

Correspondence to Felix J.B. Bäuerlein and Wolfgang Baumeister: Max-Planck-Institute of Biochemistry, Department for Molecular Structural Biology, Am Klopferspitz 18, 82152 Planegg, Germany. (F.J.B. Bäuerlein); (W. Baumeister) *baeuerlein@biochem.mpg.de (F.J.B. Bäuerlein), baumeist@biochem.mpg.de (W. Baumeister), @FelixBauerlein* 🐦 *(F.J.B. Bäuerlein).*
https://doi.org/10.1016/j.jmb.2021.167187
Edited by Sheena E Radford

Abstract

Traditionally, structural biologists approach the complexity of cellular proteomes in a reductionist manner. Proteomes are fractionated, their molecular components purified and studied one-by-one using the experimental methods for structure determination at their disposal. Visual proteomics aims at obtaining a holistic picture of cellular proteomes by studying them in situ, ideally in unperturbed cellular environments. The method that enables doing this at highest resolution is cryo-electron tomography. It allows to visualize cellular landscapes with molecular resolution generating maps or atlases revealing the interaction networks which underlie cellular functions in health and in disease states. Current implementations of cryo ET do not yet realize the full potential of the method in terms of resolution and interpretability. To this end, further improvements in technology and methodology are needed. This review describes the state of the art as well as measures which we expect will help overcoming current limitations.

© 2021 Published by Elsevier Ltd.

Introduction

The stunning performance of Deep Mind's Alpha Fold 2 in last year's CASP 14 competition,[1,2] predicting protein structure from protein sequence with accuracies almost equal to the 'gold standard' experimental methods, is seen by many as heralding a new era in structural biology. Undoubtedly, it is a triumph of Artificial Intelligence (AI) bringing a 'solution to a 50-year-old grand challenge'.[3] Experimental methods such as X-ray crystallography; nuclear magnetic resonance (NMR) and cryo-electron microscopy (cryo EM) are cumbersome to use, they can fail yielding results and they require expensive instrumentation. Computational methods are fast and less dependent on local infrastructures.

Naturally, this brings up the question whether or to what extent Alpha Fold 2, or any other future AI-based method, could make the experimental methods obsolete. Here it should be noted that Alpha Fold is not based on an ingenious fundamental solution of the protein folding problem; instead it has taken advantage of the gigantic data set of ~ 170000 protein structures deposited in the protein data bank to train its machine learning algorithms.

Furthermore, it remains to be seen how Alpha Fold performs with 'difficult' protein structures,

such as flexibly linked multidomain proteins. Or will those remain in the realm of hybrid methods to which predicted partial structures could obviously provide valuable input. So far, Alpha Fold delivers static structures, but dynamics has essential roles for function.[4] What can Alpha Fold do in cases of coexisting conformations, possibly in conjunction with molecular dynamics simulations, or will dynamics remain in the domain of experimental methods? Can AI-based methods be trained to predict structures of multisubunit molecular machines or will they remain the realm of cryo EM single particle analysis or integrative hybrid methods? Furthermore, it would be interesting to explore whether or not AI-based methods can help to illuminate the 'dark proteome' of intrinsically disordered proteins (IDPs).

Last but not least, proteins do not generally exist by themselves. In the cell they exist in crowded environments and their functions arise from manifold interactions, stable or transient, between them. The molecular architecture of cells is a largely uncharted territory so far and visual proteomics, the detailed description of cellular interaction networks is still in its infancy. Cellular or in situ cryo ET has the potential to reveal the molecular sociology of cells in near-atomic detail.[5,6] Since its beginnings, almost three decades ago[7–10] cryo ET has made slow but steady progress thanks to many advances in technology and methodology and there is still ample room for improvements. Initially, it was regarded as a low resolution method but this is changing and in favorable scenarios resolutions in the 3 Å range have been attained.[11] One should also keep in mind that resolution is an oversimplifying criterion for data quality in cryo ET. The contextual information provided by cellular tomograms can be as important as is resolution and it might be rewarding to develop measures for information density instead. We do not foresee that AI-based methods will be able to predict the molecular sociology of cells with acceptable fidelity given the sparsity of information that is available or will become available in the foreseeable future. Very likely however, AI-based methods will transform image processing and image interpretation.

In this contribution we will describe the state-of-the-art of cellular cryo ET with a focus on technology and methodology. We will highlight challenges towards high resolution visual proteomics and indicate how current limitations can be overcome.

Cryo-ET data acquisition

The typical workflow for cellular cryo electron-tomography (cryo-ET) is outlined in Figure 1 alongside some of the challenges and measures to overcome current limitations. In a nutshell, cells are either grown or deposited on grids and vitrified by rapid freezing for preservation in a close-to-native state (Figure 1a). Subcellular structures of interest are identified and located by cryo light-microscopy (cryo-LM) and their coordinates transferred to a cryo-focused ion-beam instrument (cryo-FIB) for local thinning, rendering them transparent for transmission electron microscopy (TEM) (Figure 1(b), (c)). In the cryo-TEM projection 2D images are recorded over a range of different orientations with respect the electron beam enabling the computational reconstruction of 3D volumes (Figure 1(d)). Following the correction of some resolution limiting factors, such as beam-induced motions, or denoising (Figure 1(e)), the tomograms can be analyzed further using computational methods for feature segmentation, identification (template matching) (Figure 2(c)-(e)), classification and subvolume averaging of repetitive structures (Figure 2(f)).

Specimen preparation & vitrification

The standard preparation of cellular samples for cryo-ET includes the growth on non-poisonous electron microscopy (EM) grids. Physical fixation by very rapid freezing (10^4-10^5 K/s) results in the formation of amorphous ice,[12–14] a process called vitrification. Liquid water solidifies, without reorganization into ice crystals. The latter would alter and damage biological structures by exclusion of solvents[15] and volume expansion. Vitrification preserves cellular samples in a close-to-native state, unstained, fully hydrated, and with Brownian motion at near standstill. Molecular structures are thus well preserved in their physiological state and conformation, conducive to high resolution imaging. Vitrification of small samples can be achieved by plunge-freezing[16,17] and is a well-established routine procedure.

While many cellular processes can be studied in single isolated cells, there are some important aspects of life which require to extend the workflow to tissues (Figure 1(a)). Cellular and animal models of neurodegenerative diseases for example, recapitulate only partially disease phenotypes.[18,19] This calls for the investigation of human/patient-derived tissues.[20] The development of pipelines for the investigation of tissues will pave the way to explore a wide variety of biological phenomena *in situ,* beyond the well established procedures for single isolated cells.

A critical limitation of cryo-ET is the vitrification depth, or in other words, the size of the sample (Figure 1(a)). Larger eukaryotic cells such as HeLa cells are not always fully vitrified by plunge-freezing, due to insufficient heat transfer from regions $\gtrsim$ 5 μm below the surface which results in ice crystal formation.[21] To achieve vitrification of specimens up to 200 μm in thickness; it is possible to resort to high-pressure freezing (HPF)[13,22] which uses an optimum in the phase diagram of water at 2048 bar.[23] HPF-frozen specimens however are

CRYO-ET WORKFLOW	STATE-OF-THE-ART	CHALLENGES	PERSPECTIVES
a Sample Preparation & Vitrification	• Plunge-freezing < 5 μm HPF < 200 μm • Single isolated cells	Vitrification depth Sample thickness	⟳ Cryoprotection (Glycerol) ⟳ Tissue (human biopsies)
b Cryo-CLEM	• 3D-Localization >200 nm • Separate instruments • Diffraction limited >400 nm • Fluorescent labels	Localization accuracy Efficiency / Transfers Imaging resolution Labeling	⟳ Super resolution LM ⟳ LM-Integration in cryo-FIB ⋀ Super resolution LM ◔ Chemical imaging
c Cryo-FIB	• < 10 Lamellae/d • ~ 3000 μm³/min • Lamella depth < 50 μm	Low throughput Limited volume removal Depth of region of interest	◔ Automation ◔ Plasma FIB ⟳ Cryo-Lift-Out
d Cryo-TEM	• Amplitude contrast / Volta-PP • Direct detectors • Regular operator interaction • 20-45 min / tilt-series	Low contrast (SNR) Limited DQE Low throughput Low throughput	SNR Laser-PP SNR Better cameras ◔ Automation ◔ Fast-tilt-series
e Post-Processing	• Traditional denoising procedures • Linear registration	Low contrast (SNR) Beam-induced sample deformation / motion	SNR AI-Denoising SNR Motion correction (non-linear registration)
f Visualization & Interpretation	• Template dependent • Individual detection • Hypothesis driven • Manual picking • Manual & algorithm-assisted	Visual proteomics Visual proteomics Visual proteomics Template not available Segmentation	⟳ Template free detection 0010 Large-scale data mining 0010 Bayesian approach ◔ AlphaFold ◔ AI-Segmentation

⟳ Enabling   ⋀ Resolution / Precision   SNR Data Quality   ◔ Speedup   0010 Data mining

Figure 1. State-of-the-art cryo-ET workflow with its challenges and perspectives for improvements. The first column describes the key elements of the cryo-ET workflow, with the corresponding state-of-the-art procedures in the second column. The third column outlines the main challenges of the present workflow for which the fourth column highlights the perspective of concepts tackling these challenges. For some of these concepts, first solutions have become available recently but further developments are needed for perfect solutions.
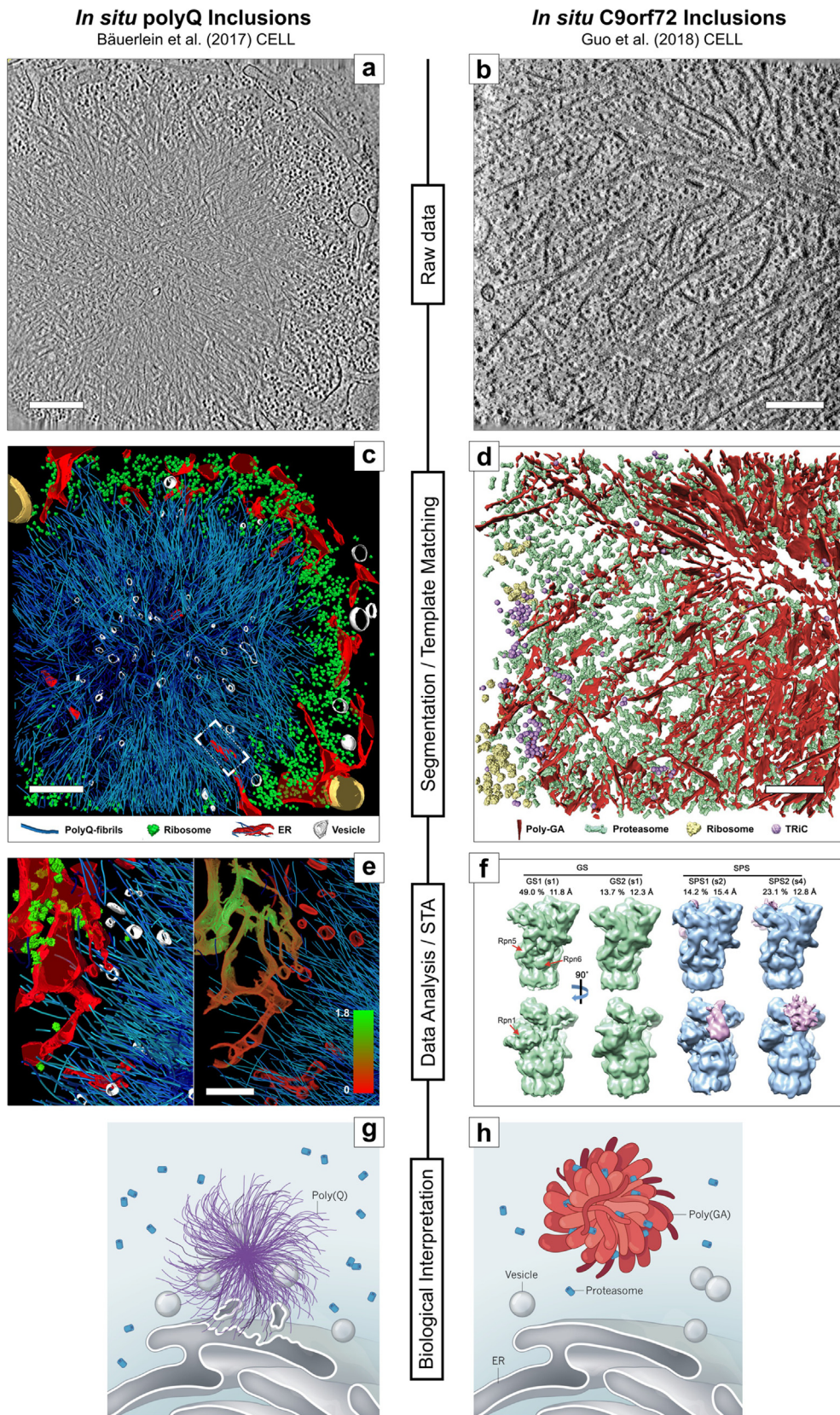
embedded in a thick block of ice; requiring elaborate correlation methods to locate features of interest and complex cryo-lift-out procedures for the preparation of the lamella. The proof-of-principle for cryo-lift-out has been demonstrated,[24–26] but this method is not yet routine and needs further automation.

An alternative approach for mammalian/human cells, that do not fully vitrify, uses a short incubation in 10% glycerol as cryoprotectant.[27] This treatment can help to achieve full vitrification and has been shown not to affect cell architecture.[27–31] Glycerol is a natural product of cells and some insects and vertebrates increase cytosolic glycerol production to survive during freezing periods.[32,33]

This simple approach also enabled the first cryo-ET visualizations of some unique features from thin Drosophila tissues.[34] However concentrations and incubation times need to be optimized and other membrane-permeant cryoprotectants should be explored.

Targeting and identification by cryo-correlative microscopy (Cryo-CLEM)

The idea of using correlative approaches came up in the late 1970s.[35] It takes advantage of complementary microscopy techniques that allow to identify certain cells within a population of cells;

In situ polyQ Inclusions
Bäuerlein et al. (2017) CELL

In situ C9orf72 Inclusions
Guo et al. (2018) CELL

containing the features of interest followed by the targeted acquisition of high-resolution data. More recently this concept has been used in cryo-EM. Correlative light and cryo electron-microscopy (cryo-CELM) combines the power of identification by fluorescently labeled structures and the high-resolution information of cryo electron microscopy.[36,37] Cryo-CLEM may serve different purposes: i) the targeting/localization of structures of interest to guide cryo-FIB lamella preparation ensures, that the final electron transparent lamella (<200–300 nm) contains the structure of interest. And ii) the identification of subcellular structures in the tomogram with high fidelity and accuracy. The localization of subcellular features is challenging because the volume of a eukaryotic cell (several thousand μm^3) is much larger than the volume of a tomogram (<1 μm^3). The probability of capturing multiple copies of a given protein in a tomogram depends on its abundance and local concentration in the cell, which may vary from a handful[38] to thousands of copies.[39] In single-particle cryo-EM; abundance is not an issue because the molecules of interest are purified and concentrated such that the number of copies for averaging is essentially unlimited. Certain events or subcellular structures may be spatially very localized and are not trivial to be identified as for example intermediates in autophagosome biogenesis. It is sometimes necessary to identify a subpopulation of cells that contains a feature of interest such as neurotoxic protein aggregates that are found only in a few cells amongst a population of several thousands (Figure 2(a)-(h)). Cryo-CLEM has been applied in several studies in the recent years with diffraction limited light microscopy (LM).[27–29,40–44] Abundant proteins such as ribosomes can be found in tomograms acquired in almost any subcellular location; whereas rare targets require elaborate localization and targeting procedures.

The main challenge in localizing a structure of interest is to precisely correlate and superimpose the coordinate systems of the 3D data of the LM and the cryo-FIB data. This can be achieved, using markers that are visible in all microscope modalities (LM, FIB). Fluorescently labeled structures can be localized inside a cellular volume by 3D correlation with an accuracy of 200–300 nm in many cases[45] (Figure 1(b)). While the localization accuracy of a fiducial-based approach is not limited by the resolution of the LM, it can be challenging to fit the centers of the fiducial markers in all modalities. Another issue is the need to transfer the sample between the LM and the cryo-FIB instrument. This not only limits throughput, it also bears the risk of introducing sample deformations affecting localization accuracy. Ice crystal contamination can easily occur, hindering lamella preparation in the cryo-FIB. The integration of a widefield LM into the cryo-FIB instrument has been recently done[46] and first setups are commercially available. This simplifies the handling and

Figure 2. Cryo-ET studies of neurotoxic protein aggregates in situ. **(a)** Tomographic slice (2.8-nm thick) of an inclusion body (IB) in an Htt97Q-GFP-transfected mouse primary neuron. A dense network of thin poly-Q fibrils is visible. **(b)** Tomographic slice (5-nm thick) of an inclusion body in a (GA)$_{175}$-GFP-transduced mouse neuron. A dense network of thick poly-GA-GFP ribbons is visible. **(c)** 3D rendering of the tomogram in (a), showing radially oriented fibrils of the IB, strongly interacting with surrounding membranes of the ER and vesicles trapped inside the fibrillar network. ER membranes (red), Htt97Q-GFP fibrils (cyan), ribosomes (green), vesicles (white), and mitochondria (gold). Note that the core of the IB is largely devoid of ribosomes and other macromolecular complexes, which are found at the IB periphery. **(d)** 3D rendering of the tomogram in (b), showing different macromolecules found either within or at the periphery of the aggregate. Poly-GA ribbons (red), 26S proteasomes (green), ribosomes (yellow), TRiC/CCT chaperonins (purple). **(e)** Left: 3D rendering of ER membranes and ER-bound ribosomes in the vicinity of Htt97Q fibrils. Note that most ribosomes are liberated from ER membranes directly interacting with Htt97Q fibrils. Right: Visualization of the density-map of membrane-bound ribosomes in the area shown on the left (red/green indicates low/high local ribosome-densities). **(f)** 26S proteasomes, classified according to their regulatory particle conformation into ground- or substrate-processing states, showing two ground states (GS1, GS2) and two substrate-processing classes (SPS1, SPS2). The four density maps are displayed in a solid surface representation in two different views. Prominent densities (pink) in the substrate binding region of SPS1 and SPS2 which cannot be assigned to the proteasome density are interpreted as substrate. **(g)** Tracts of the amino acid glutamine (poly(Q) tracts), which are associated with Huntington's disease, form fibrillar aggregates. These aggregates deform and rupture the membranes of the ER and lead to local impairments of the ER organization. Thus the interaction of these fibrils with cellular endomembranes are suggested to contribute to cytopathology beyond the toxic role of oligomers. **(h)** In some cases of the neurodegenerative disorder amyotrophic lateral sclerosis, long chains of glycine and alanine amino-acid residues (poly(GA) tracts) aggregate in neurons. Poly(GA) tracts form ribbon-like aggregates that trap proteasomes, which are needed for the degradation of unwanted proteins. Proteasome stalling and compromising protein quality control provides an explanation for the toxicity of this aggregate. The observations suggest different aggregates cause neurodegeneration through different mechanisms. Scale bars in (a),(c) 400 nm, in (e) 250 nm, in (b),(d) 200 nm.(a)-(f) with permission from Elsevier. (g),(h) with permission from Springer Nature.

the efficiency of the correlated lamella-preparation. The localization accuracy however is not likely to be substantially improved by this approach.

The precision and efficiency of lamella preparation would benefit from the integration of a super-resolution LM into the cryo-FIB. An interesting approach that relies on the technology of point-spread-function engineering may enable improved localization (particularly in the z-direction) and identification accuracies of < 100 nm.[47–51] Another strategy to correlate and superimpose the coordinate systems of the LM and the cryo-FIB could be using the fixed spatial relationships in the integrated cryo-FIB/LM instrument – for this however precise piezo-stages would be needed. Another limitation of LM methods for cryo-CLEM is the restricted color choice of fluorescent labels; since methods like DNA-paint[52] are not applicable to vitrified specimens. Subcellular structures could also be targeted by spatially resolved chemical imaging in the cryo-FIB. Integrated time-of-flight secondary ion mass spectrometry (TOF-SIMS) and energy dispersive spectroscopy (EDS) are established in the material sciences and may be adapted to biological specimens. EDS can locate targets in some 100 nm depth with limited sensitivity (>1000 ppm) and TOF-SIMS analyzes the cellular content removed by the focused ion-beam with higher sensitivity (>10 ppm) and may indicate, when the target has been hit. It needs to be determined, whether or not the sensitivity will be sufficient for vitrified biological samples.

The complexity of cellular proteomes makes it challenging to determine the molecular identity of features visible in the tomograms. High-precision cryo-CLEM correlation has the potential to assign and identify electron densities. While the localization accuracy is not necessarily limited by the resolution of the LM,[45,53,54] the ability to unequivocally identify structures via a cryo-CLEM approach is compromised by diffraction-limited LM (~400 nm[55–57]). If the fluorescent signals are well separated as sparse isolated spots, 2D localization and correlation approaches for cryo-CLEM can yield a correlation accuracy of 50–100 nm.[40,53,54,58] In other cases however, the advantage of super-resolution LM (SR-LM) methods of reaching resolutions down to well below 100 nm make them very attractive to adapt and integrate them into the cryo-ET workflow.[57,59]

Several SR-LM concepts have been explored under cryo conditions. The suitability of single molecule localization microscopy techniques (SMLM) for cryo-CLEM[60–65] has been demonstrated and resulted in a structural resolution of 74–125 nm and a localization accuracy of 13–40 nm. However these studies also highlighted a major problem of super-resolution cryo-CLEM; namely the risk of devitrification of specimens due to the high laser intensities needed (SMLM $\sim 10^3$–10^4 W/cm^2).[66] Stimulated emission depletion

(STED) can reach high resolution but requires even higher laser intensities ($\sim 10^3$–10^5 W/cm^2).[66] Super-resolution optical fluctuation imaging (SOFI) is a low-dose imaging scheme ($\sim 10^2$ W/cm^2) compared to STED and SMLM and has been applied[67,68] without indications of devitrification and achieved a resolution ~135 nm. Cryo-structured illumination microscopy (SIM)[69] uses the lowest laser intensities ($<10^2$ W/cm^2)[66] but has not reached resolutions below 210 nm so far. A limiting factor are the LM objectives: so far exclusively air objectives are available for cryo-conditions which have inherently low numerical apertures (NA) reducing the efficiency to collect photons and therefore necessitate higher laser intensities. First cryo-immersion setups with high NA have been developed but are so far suffering from aberrations[70,71] and therefore could not substantially improve the resolution.[71]

To achieve the goals of visual proteomics, SR-LM methods are needed to complement the cryo-CLEM workflow. Further systematic studies of acceptable photon doses and dose rates are necessary to establish imaging schemes, that ensure maintenance of the vitrified state of the sample. The development of LM cryo-immersion objectives with high NA, low aberrations and importantly also NA-adapted immersion media (that still need to be identified) would help to lower the necessary photon dose. A rather new SR-method called 'MINFLUX'[72] seems to be a promising candidate for cryo-CLEM: MINFLUX offers the highest precision of all SR approaches with single-digit isotropic nanometer localization precision.[73] Furthermore MINFLUX requires much fewer emitted photons than PALM/STORM. This would allow to identify features in tomograms by correlation with individual fluorescently labeled proteins.

In contrast to these deterministic ways of protein identification also probabilistic/Bayesian and label-free approaches may guide the identification of proteins. Quantitative mass spectrometry is able to provide a ground truth as to the abundance of a given protein and hereby create expectation values to find certain protein species in the tomogram. For this also the proteome and transcriptome of cellular sub volumes could be analyzed, by isolating these with the cryo-FIB and by subsequent mass spectrometry. Such investigations could guide experiments, by providing critical information in assessing the feasibility of an experiment.

Throughput of the cryo-ET workflow

A major limitation of cryo-ET is the thickness of samples. With today's intermediate-voltage electron microscopes, high-resolution data can only be acquired with a sample thickness well below 500 nm. Since eukaryotic cells are typically ten times thicker, they need to be thinned down to

become electron transparent. Therefore, after having identified cells, containing the structures of interest and their subcellular location by cryo-CLEM, the frozen hydrated cells are subjected to FIB milling, a gentle procedure for ablating material.[74,75] A focused gallium ion-beam removes parts of the cell above and below the structure of interest, creating a thin lamella across the cell. Following transfer to a cryo-TEM, micrographs are recorded in the form of tilt series for 3D reconstruction.

The transfer of frozen hydrated specimens between the different microscopes comes with the risk of becoming contaminated by ice crystals derived from the atmospheric humidity, hindering lamella-preparation. Tools and procedures have been developed to minimize the risk of contamination.[76,77] The integration of a LM into the cryo-FIB, as mentioned in the previous section, will not only eliminate a contamination-prone step but also improve throughput.

Another throughput-limiting factor is the positioning of cells on EM grids: a substantial portion of adherent cells spreading on EM grids is inaccessible to cryo-FIB lamella milling, when located on or close to the metal bars of the EM grid. This becomes particularly limiting, if the target of interest is found only in a subpopulation of cells. A new approach of photo-micropatterning allows spatially controlled cell adhesion on EM grids[78,79] avoiding this problem.

Many steps in the cryo-ET workflow are complex, technically challenging and time-consuming. The throughput along the whole workflow could be accelerated by automation. A major bottleneck is the laborious and largely manual cryo-FIB lamella-preparation. First concepts for automating lamella preparation[80,82] have been proposed. The ability to remove material (sputter yield) with the cryo-FIB is limited by the ion current. This is a critical limitation, when the goal is to produce lamellas from volumes deep inside tissues. FIB-instruments using an inductively coupled plasma source (plasma-FIB) are capable of delivering ion currents more than a magnitude higher: up to 2500 nA versus 65 nA on traditional liquid metal Ga^+-ion sources. A first study demonstrated the applicability of an oxygen plasma-FIB on resin-embedded tissue samples.[83]

First attempts to automate the correlation procedures between the different microscopes have been published.[84] At the level of the cryo-TEM, automation of the tilt-series acquisition has been established over 15 years ago with the development of the SerialEM software package.[85] However, to acquire multiple automated and unsupervised tilt-series (batch-tomography), only a first proof-of-principle study has been published.[86] Efforts are underway to refine this concept to establish a robust batch-tomography pipeline.

At the level of the cryo-TEM, throughput could be further increased by the accelerated acquisition of the tilt-series. Currently, the acquisition of a typical tilt-series takes about 20–40 min depending on the tilt schemes being used. It involves recurrent steps of tilting the stage, tracking the acquisition area, focusing, drift-settling and eventually recording the electron micrograph. Some of these steps are time-consuming and could be optimized or skipped altogether by a priori knowledge of the stage characteristics. Taking this idea to its extremes, even a stroboscopic recording of the electron micrographs during continuous tilting of the stage might become possible, a strategy well known from x-ray crystallography[87] and computed tomography. In the end, the acquisition of a tilt series may only take seconds to a few minutes. Several groups are working along those lines and have acquired tomograms taken with fast-tilt acquisition schemes.[88]

Data quality of cryo-electron tomograms

Two image properties define the quality of cryo-ET data: contrast and resolution. In cryo-electron microscopy the signal-to-noise ratio (SNR) is necessarily low because of the radiation sensitivity of ice-embedded materials and the need to minimize their exposure to the beam. During recording the tilt series electron-beam induced structural damage[89] accumulates; limiting the final resolution.[90,91] High-resolution information is better preserved in the early projections of the tilt-series than in the later ones. Accordingly, tilt-schemes have been established that distribute the dose symmetrically over the tilt range[92] and have been shown to result in improved resolution.[93]

Contrast is generated in two ways: on the one hand there is amplitude contrast, on the other hand, there is phase contrast that has its origin in the phase-shift of the electrons' wave function while being elastically scattered by the sample. Frozen-hydrated specimens are mainly phase objects, only ~15% is contributed by amplitude contrast.[94] Taking advantage of the phase component; image contrast can be significantly increased by using phase plates such as the Volta phase plate (VPP).[95,96] The focused electron beam causes locally a surface potential on a thin carbon film which produces a dose-dependent phase shift between the unscattered and scattered parts of the electron wave.

Usage of the VPP is more important for cryo-ET than for single-particle analysis (SPA), because the options for averaging are more limited. Moreover, the improved SNR facilitates the detection and identification of small structures in crowded cellular environments. However, it comes with a cost: while the VPP increases image contrast, there is some evidence that it also leads to a weakening of signal at higher resolutions.[97] This effect remains unexplained so far but leads to a tradeoff between

contrast and resolution when utilizing the VPP. Sometimes; charging is observed when using the VPP in conjunction with lamellae. Maximizing resolution is often considered being the only goal, however achieving a good SNR is at least as important since biologically relevant information can often be derived from high-contrast medium resolution data already[21,27,98,99] (Figure 2(**a**)-(**h**)).

While the VPP has proven advantages, it would be desirable to have a phase plate without a mass in the beam path, causing some electron loss. A new concept, for which proof of principle has been demonstrated, uses a high-intensity continuous-wave laser beam to change the phase of the electron beam – the laser phase plate (LPP).[100] Such a LPP provides a stable and fine-tunable phase shift without electrostatic charging or unwanted electron scattering. This is a very promising approach and should be explored further. An optimal LPP may be combined with a spherical aberration corrector and an electron beam monochromator. Such an elec-

tron microscope would yield a nearly-ideal contrast transfer function and allow extracting a maximum of information – however at some monetary expense.

Removing resolution-limiting factors post acquisition

While every effort should be made to optimize data quality in the process of image acquisition, there is still a need to remove resolution-limiting factors post acquisition. To improve the ability to recognize features in noisy, low-contrast tomograms post acquisition, the level of noise can be reduced by computational denoising filters. Typical denoising procedures like low-pass, gaussian, median, non-linear anisotropic diffusion[101] or non-local means[102] filters have the disadvantage to introduce some blurring or may even give rise to artifacts. Deconvolution filters can increase image contrast (Figure 3(**b**)), but they
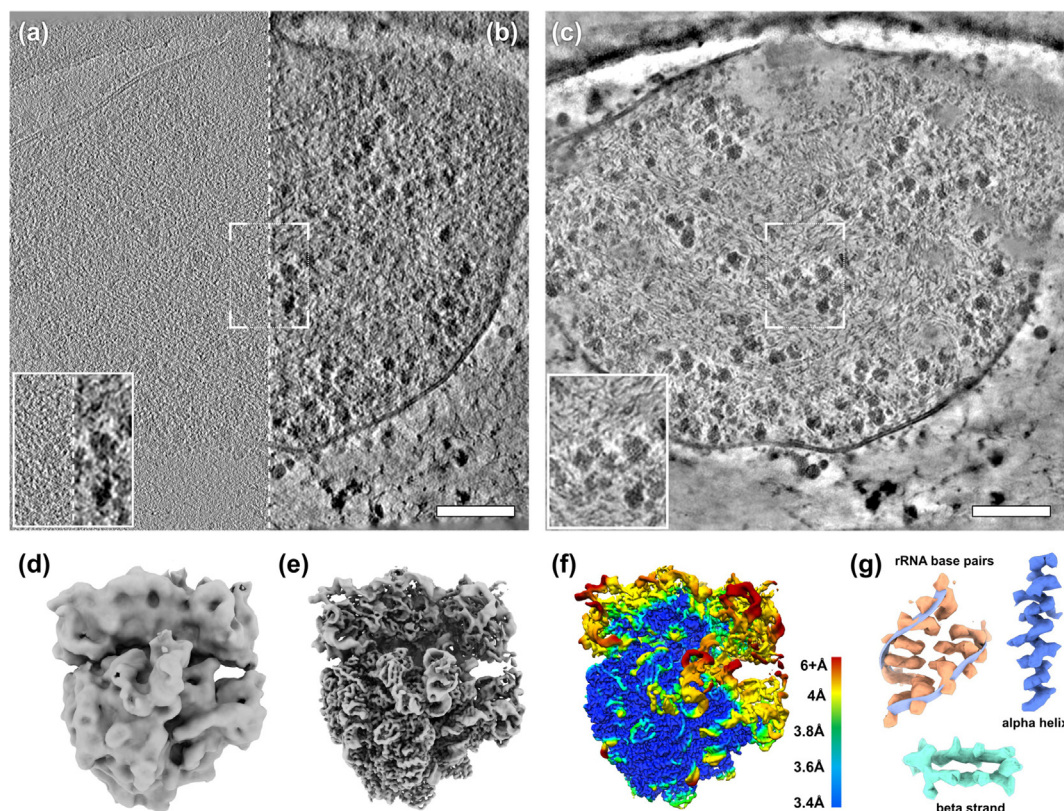

Figure 3. AI-Denoising and post-acquisition motion-correction significantly improve contrast and resolution. **(a)-(c)** Identical 0.68 nm-thick slice of a Mycoplasma pneumoniae cellular tomogram, showing the difference of traditional and AI-denoising procedures. The insets show a magnification of the indicated regions. **(a)** Original tomogram low-pass filtered (cutoff: 0.35, sigma 0.035). **(b)** Deconvolution filtered as applied in Warp.[103] **(c)** Neural network based denoising in Warp/M.[11] **(d)** A sub-tomogram average of 70S ribosomes extracted from tomograms of intact M. pneumoniae. **(e)** Reconstruction of the 70S ribosomes from the same tomograms as in (d) after multi-particle refinement in M. **(f)** Local resolution map for the map in (f). **(g)** Magnified regions of (e) showing RNA base pairs (orange), an alpha-helix (blue) and beta-strands (cyan). Scale bars in (a)-(c) 100 nm. (courtesy of Liang Xue and Julia Mahamid).

maintain a high level of noise rendering the visual interpretation of crowded environments difficult.[103]

Machine learning approaches, in particular deep learning, have become increasingly popular in the field of fluorescence microscopy[104] and have recently also been applied to cryo-ET data (Figure 3 (c)).[11,105,106] Typically, such deep neural networks are trained on high and low quality data which means in the context of denoising, high and low SNR. For cryo-ET data this is problematic, since a higher SNR comes with increased exposures of the electron beam and consequently more radiation damage. In such a scenario the network would be trained not only with noise but also with aspects of radiation damage, which could result in the elimination of high-resolution features. A new concept, called Noise2Noise[107] seeks to overcome this limitation. Independent sets of noisy micrographs of the same feature are used to train the network.[105] To this end, the data set which is recorded as a movie of multiple short exposures is divided into an even and odd set, and the average of each set represents two independent noisy images containing the same signal. The influence of radiation damage should thus be very similar in the two final images and ideally the only difference is the camera shot noise, with which the deep neural network is trained.

The application of denoising cryo-ET data by deep learning is in its beginnings and needs to be further analyzed, also with an assessment of possible artefacts. In principle this approach has great potential, since denoising by neural networks would allow to acquire tomograms with lower electron doses, and thereby less damage. Denoising greatly facilitates the segmentation of tomograms and the identification of features.

As the micrographs are taken, image blurring is caused by sample motions, a critical resolution-limiting factor. Two types of motion can be distinguished: global drift due to imperfections of the microscope's specimen stage and electron beam-induced motion. The global drift of the sample can be measured and corrected for in the subframes of images taken in the form of movies.[108,109] For the tomographic reconstruction, the 2D projections of the tilt-series need to be aligned with respect to each other. This is usually achieved by linear registration, which considers the sample to be a rigid body, with translational and rotational transformations. It has been shown however, that upon imaging the irradiation causes electron beam-induced motions and anisotropic deformations of the sample.[91,110] This implies that the sample should not be considered as a rigid body and that these complex sample deformations including warping and doming call for non-linear registration approaches.[111,112] Several algorithms have been developed for subtomogram averaging, that consider each particle's trajectory individually.[113–116] However in the context

of the complex non-linear sample deformations, it is beneficial to consider the individual particles in a tomogram not separately but rather as a multi-particle system in the same physical space.[11] This idea has been implemented and resulted in significantly improved resolution[11] (Figure 3(d)-(g)). Similarly, the alignment information of the individual subvolumes may be used to refine the alignment of the entire tilt-series. Instead of fiducial markers, which are for practical reasons difficult to use with eukaryotic systems, high contrast intrinsic features such as ribosomes can be used for refining the alignment. Deep neural networks may help to improve the alignment of the tilt-series by the ability to identify suitable landmarks.[117] After the application of the aforementioned denoising approaches, practically all available alignment procedures will lead to significantly improved results.

Identification and visualization of structures

Cryo-electron tomograms depict cellular landscapes in their full and often bewildering complexity. Their interpretation is challenged by data quality, in particular resolution and SNR, but also by the crowded nature of cellular volumes with a plethora of molecular species inhabiting them.

A first step in the visualization and description of cellular tomograms is usually the segmentation of membranes and filamentous structures (Figure 2(c)-(e)).[21,27,28,118–122] Manual segmentation is not only time-consuming, it is also unsatisfactory because there is always an element of subjectivity. This is mainly caused by the limited tilt range, which leaves an incomplete angular sampling in Fourier-space, called missing wedge, introducing elongation and ray artifacts. Calling for automation, membrane detection algorithms have been developed, based on tensor voting,[123] but some manual intervention is still needed. Membrane segmentation can guide and constrain the localization of membrane proteins, comprising about a third of the human proteome. Algorithms have also been developed for the tracing of filaments[102,124] but their precision is still not as good as it ought to be. It can be expected, that pattern recognition by deep learning algorithms will further improve automated segmentation.

Macromolecules can be localized and identified in tomograms by template matching (TM)[125] using a priori known reference structures (Figure 2(c)-(e)), typically derived from experimentally determined high-resolution structures. Experimental molecular structures that could be used for TM are currently available for only a third of the human proteome. AlphaFold2 could in the future contribute to the data

base useful for TM. But a limitation that remains in the size of detectable targets. Matching structures extracted from the tomograms can be subjected to image classification. This allows to exclude false-positive hits and to separate *in silico* coexisting conformers. The members of the differentiated classes can be averaged to obtain 3D representations of the structures of interest with improved resolution and SNR, a process referred to as subtomogram averaging (Figure 2(**f**)). Several software packages have been developed for subtomogram averaging: Protomo,[126] PEET,[127] PyTom,[128] EMAN2,[129] RELION,[130] Dynamo,[131] emClarity[113] and STOPGAP.[132]

Limitations in sensitivity mean that not all particles of a certain molecular species may be detected. Also the template may not well represent the *in situ* structure and conformation. The detection and identification of complexes smaller than ∼ 400 kDa can be challenging, given the quality of tomograms due to the attenuation of the high-resolution signal in the three-dimensional reconstructions. Radiation damage, as discussed earlier and strong defocusing are key aspects, limiting resolution. Strong defocusing is necessary to have sufficient low-frequency contrast for the tilt-series alignment; this, in turn dampens the high-resolution signal and thus limits the detection efficiency.[133] Therefore it has been proposed to apply TM to 2D data,[134] while exposure is much lower than for the recording of a full tilt-series and damage is thereby minimized. By acquisition close to focus, high-resolution information can be maintained.[133] The 2D-TM approach becomes problematic however with increasing sample thickness. A hybrid of 2D-TM and 3D-TM approach may be an option to consider in the future for the interpretation of tomograms.

TM is a hypothesis-driven approach to search for specific proteins in tomograms. Cryo-ET visualizes the cellular landscape in its macromolecular entirety. Therefore a holistic approach to locate and identify proteins in a large-scale data mining attempt would be highly desirable. A template-free image-processing procedure, able to accurately detect densities in cryo electron tomograms has recently shown to be able to locate and classify membrane-associated complexes of ∼ 200 kDa.[135] Machine learning methods like neural networks have proven their potential to identify and eliminate noise.[11,105,106] For cellular tomograms, deep neural networks were able to localize multiple macromolecular species simultaneously and significantly faster than with TM.[136,137] Expanding on this idea, deep neural networks could be trained, self-supervised on large numbers of tomograms, that have been deposited on data-bases like EMDB,[138] EMPIAR,[139] and ETDB.[140] This would facilitate the creation of cellular molecular atlases and help paving the way for visual proteomics.

Concluding remarks and future perspectives

Visual proteomics by cryo-electron tomography has the potential to generate comprehensive molecular maps of cellular landscapes. It is a label-free method depicting cellular volumes in a close-to-native state with subnanometer resolution. So far, this is largely uncharted territory and therefore the discovery potential is huge. To realize the full potential of cryo-ET, further advances in technology and methodology must be made from sample preparation to data acquisition and data interpretation. Density maps of cellular volumes are rich in information but mining this information is very challenging given their crowdedness. It is expected that the in the future, AI-based methods will transform image processing and aid the interpretation of tomograms.

CRediT authorship contribution statement

Felix J.B. Bäuerlein: Conceptualization, Writing – review & editing. **Wolfgang Baumeister:** Conceptualization, Writing – review & editing.

Declaration of Competing Interest

The authors declare that they have no known competing financial interests or personal relationships that could have appeared to influence the work reported in this paper.

Cryo-focused-ion beam; Cryo-TEM, Transmission electron microscope; LPP, Laser phase plate; SMLM, single molecule localization microscopy techniques; VPP, Volta phase plate

References

1. Callaway, E., (2020). 'It will change everything': DeepMind's AI makes gigantic leap in solving protein structures. *Nature*, **588**, 203–204.

2. Kinch, L., Kryshtafovich, A., Schaefer, R., Grishin, N., (2021). Topological evaluation of difficult targezs in the 14th round of critical assessment of protein structure preiction (CASP14). *In press*,.

3. DeepMind, https://deepmind.com/blog/article/alphafold-a-solution-to-a-50-year-old-grand-challenge-in-biology, 2020.

4. Alderson, T.R., Kay, L.E., (2021). NMR spectroscopy captures the essential role of dynamics in regulating biomolecular function. *Cell*, **184**, 577–595.

5. Nickell, S., Kofler, C., Leis, A.P., Baumeister, W., (2006). A visual approach to proteomics. *Nat. Rev. Mol. Cell Biol.*, **7**, 225–230.

6. Beck, M., Baumeister, W., (2016). Cryo-electron tomography: can it reveal the molecular sociology of cells in atomic detail? *Trends Cell Biol.*, **26**, 825–837.

7. Dierksen, K., Typke, D., Hegerl, R., Koster, A.J., Baumeister, W., (1992). Towards automatic electron tomography. *Ultramicroscopy*, **40**, 71–87.

8. Dierksen, K., Typke, D., Hegerl, R., Baumeister, W., (1993). Towards automatic electron tomography II. Implementation of autofocus and low-dose procedures. *Ultramicroscopy*, **49**, 109–120.

9. Dierksen, K., Typke, D., Hegerl, R., Walz, J., Sackmann, E., Baumeister, W., (1995). Three-dimensional structure of lipid vesicles embedded in vitreous ice and investigated by automated electron tomography. *Biophys. J.*, **68**, 1416–1422.

10. Robinson, C.V., Sali, A., Baumeister, W., (2007). The molecular sociology of the cell. *Nature*, **450**, 973–982.

11. Tegunov, D., Xue, L., Dienemann, C., Cramer, P., Mahamid, J., (2021). Multi-particle cryo-EM refinement with M visualizes ribosome-antibiotic complex at 3.5 A in cells. *Nat. Methods*, **18**, 186–193.

12. Moor, H., (1964). Die Gefrier-Fixation lebender Zellen und ihre Anwendung in der Elektronenmikroskopie. *Zeitschrift für Zellforschung und Mikroskopische Anatomie*, **62**, 546–580.

13. Moor, H., Riehle, U., (1968). Snap-freezing under high pressure: A new fixation technique for freeze-etching. *Proc 4th Eur Reg Conf Electron Microsc, Rome*, **2**, 33–44.

14. Riehle, U., Höchli, M., (1973). *The theory and technique of high pressure freezing. Freeze-Etching. Techniques and Applications*,. Societe Francais de Microscopie Electronique, pp. 31–61.

15. Heuser, J., (2002). Whatever happened to the 'microtrabecular concept'? *Biol. Cell*, **94**, 561–596.

16. Dubochet, J., McDowall, A.W., (1981). Vitrification of pure water for electron microscopy. *J. Microsc.*, **124**, 3–4.

17. Dubochet, J., Adrian, M., Chang, J.-J., Homo, J.-C., Lepault, J., McDowall, A.W., et al., (1988). Cryo-electron microscopy of vitrified specimens. *Q. Rev. Biophys.*, **21**, 129–228.

18. Dawson, T.M., Golde, T.E., Lagier-Tourenne, C., (2018). Animal models of neurodegenerative diseases. *Nat. Neurosci.*, **21**, 1370–1379.

19. Barker, R.A., Bjorklund, A., (2020). Animal models of Parkinson's disease: are they useful or not? *J. Parkinsons Dis.*,.

20. Bäuerlein, F.J.B., Fernandez-Busnadiego, R., Baumeister, W., (2020). Investigating the structure of neurotoxic protein aggregates inside cells. *Trends Cell Biol.*, **30**, 951–966.

21. Mahamid, J., Pfeffer, S., Schaffer, M., Villa, E., Danev, R., Cuellar, L.K., et al., (2016). Visualizing the molecular sociology at the HeLa cell nuclear periphery. *Science*, **351**, 969–972.

22. Studer, D., Humbel, B.M., Chiquet, M., (2008). Electron microscopy of high pressure frozen samples: bridging the gap between cellular ultrastructure and atomic resolution. *Histochem. Cell Biol.*, **130**, 877–889.

23. Kanno, H., Speedy, R.J., Angell, C.A., (1975). Supercooling of water to -92°C under pressure. *Science*, **189**, 880–881.

24. Mahamid, J., Schampers, R., Persoon, H., Hyman, A.A., Baumeister, W., Plitzko, J.M., (2015). A focused ion beam milling and lift-out approach for site-specific preparation of frozen-hydrated lamellas from multicellular organisms. *J. Struct. Biol.*, **192**, 262–269.

25. Schaffer, M., Pfeffer, S., Mahamid, J., Kleindiek, S., Laugks, T., Albert, S., et al., (2019). A cryo-FIB lift-out technique enables molecular-resolution cryo-ET within native Caenorhabditis elegans tissue. *Nat. Methods*, **16**, 757.

26. Parmenter, C.D., Nizamudeen, Z.A., (2021). Cryo-FIB-lift-out: practically impossible to practical reality. *J. Microsc.*, **281**, 157–174.

27. Bäuerlein, F.J.B., Saha, I., Mishra, A., Kalemanov, M., Martinez-Sanchez, A., Klein, R., et al., (2017). In situ architecture and cellular interactions of PolyQ inclusions. *Cell*, **171** (179–87) e10.

28. Guo, Q., Lehmer, C., Martinez-Sanchez, A., Rudack, T., Beck, F., Hartmann, H., et al., (2018). In situ structure of neuronal C9orf72 Poly-GA aggregates reveals proteasome recruitment. *Cell*, **172** (696–705) e12.

29. Trinkaus, V.A., Riera-Tur, I., Martinez-Sanchez, A., Bauerlein, F.J.B., Guo, Q., Arzberger, T., et al., (2021). In situ architecture of neuronal alpha-Synuclein inclusions. *Nat Commun.*, **12**, 2110.

30. Sousa, R., (1995). Use of glycerol, polyols and other protein structure stabilizing agents in protein crystallization. *Acta Crystallogr. D Biol. Crystallogr.*, **51**, 271–277.

31. Ye, J.H., Zhang, J., Xiao, C., Kong, J.Q., (2006). Patch-clamp studies in the CNS illustrate a simple new method for obtaining viable neurons in rat brain slices: glycerol replacement of NaCl protects CNS neurons. *J. Neurosci. Methods*, **158**, 251–259.

32. Zachariassen, K.E., (1985). Physiology of cold tolerance in insects. *Physiol. Rev.*, **65**, 799–832.

33. Rexer-Huber, K.M., Bishop, P.J., Wharton, D.A., (2011). Skin ice nucleators and glycerol in the freezing-tolerant frog Litoria ewingii. *J. Comp. Physiol. B.*, **181**, 781–792.

34. Bäuerlein, F.J.B., Pastor-Pareja, J.C., Fernández-Busnadiego, R., (2021). Cryo-electron tomography of native Drosophila tissues vitrified by plunge freezing. *bioRxiv*,. https://doi.org/10.1101/2021.04.14.437159.

35. Webster, R.E., Osborn, M., Weber, K., (1978). Visualization of the same PtK2 cytoskeletons by both immunofluorescence and low power electron microscopy. *Exp. Cell Res.*, **117**, 47–61.

36. Sartori, A., Gatz, R., Beck, F., Rigort, A., Baumeister, W., Plitzko, J.M., (2007). Correlative microscopy: Bridging the gap between fluorescence light microscopy and cryo-electron tomography. *J. Struct. Biol.*, **160**, 135–145.

37. Schwartz, C.L., Sarbash, V.I., Ataullakhanov, F.I., Mcintosh, J.R., Nicastro, D., (2007). Cryo-fluorescence microscopy facilitates correlations between light and cryo-electron microscopy and reduces the rate of photobleaching. *J. Microsc.*, **227**, 98–109.

38. Fukuda, Y., Beck, F., Plitzko, J.M., Baumeister, W., (2017). In situ structural studies of tripeptidyl peptidase II (TPPII) reveal spatial association with proteasomes. *Proc. Natl. Acad. Sci.*, **114**, 4412–4417.

39. Freeman Rosenzweig, E.S., Xu, B., Kuhn Cuellar, L., Martinez-Sanchez, A., Schaffer, M., Strauss, M., et al., (2017). The eukaryotic CO2-concentrating organelle is liquid-like and exhibits dynamic reorganization. *Cell*, **171** (148–62) e19.

40. Hampton, C.M., Strauss, J.D., Ke, Z., Dillard, R.S., Hammonds, J.E., Alonas, E., et al., (2017). Correlated fluorescence microscopy and cryo-electron tomography of virus-infected or transfected mammalian cells. *Nat. Protoc.*, **12**, 150–167.

41. Mahamid, J., Tegunov, D., Maiser, A., Arnold, J., Leonhardt, H., Plitzko, J.M., et al., (2019). Liquid-crystalline phase transitions in lipid droplets are related to cellular states and specific organelle association. *Proc. Natl. Acad. Sci. U. S. A.*, **116**, 16866–16871.

42. Metskas, L.A., Briggs, J.A.G., (2019). Fluorescence-based detection of membrane fusion state on a cryo-EM grid using correlated cryo-fluorescence and cryo-electron microscopy. *Microsc. Microanal.*, **25**, 942–949.

43. Wilfling, F., Lee, C.W., Erdmann, P.S., Zheng, Y., Sherpa, D., Jentsch, S., et al., (2020). A selective autophagy pathway for phase-separated endocytic protein deposits. *Mol. Cell.*, **80**, (764–78) e7

44. Klein, S., Wimmer, B.H., Winter, S.L., Kolovou, A., Laketa, V., Chlanda, P., (2021). Post-correlation on-lamella cryo-CLEM reveals the membrane architecture of lamellar bodies. *Commun. Biol.*, **4**, 137.

45. Arnold, J., Mahamid, J., Lucic, V., de Marco, A., Fernandez, J.-J., Laugks, T., et al., (2016). Site-specific cryo-focused ion beam sample preparation guided by 3D correlative microscopy. *Biophys. J.*, **110**, 860–869.

46. Gorelick, S., Buckley, G., Gervinskas, G., Johnson, T.K., Handley, A., Caggiano, M.P., et al., (2019). PIE-scope, integrated cryo-correlative light and FIB/SEM microscopy. *Elife*, **8**

47. Pavani, S.R., Thompson, M.A., Biteen, J.S., Lord, S.J., Liu, N., Twieg, R.J., et al., (2009). Three-dimensional, single-molecule fluorescence imaging beyond the diffraction limit by using a double-helix point spread function. *Proc. Natl. Acad. Sci. U. S. A.*, **106**, 2995–2999.

48. Backer, A.S., Moerner, W.E., (2014). Extending single-molecule microscopy using optical Fourier processing. *J. Phys. Chem. B.*, **118**, 8313–8329.

49. Shechtman, Y., Weiss, L.E., Backer, A.S., Lee, M.Y., Moerner, W.E., (2016). Multicolour localization microscopy by point-spread-function engineering. *Nat. Photonics.*, **10**, 590–594.

50. Hershko, E., Weiss, L.E., Michaeli, T., Shechtman, Y., (2019). Multicolor localization microscopy and point-spread-function engineering by deep learning. *Opt. Express.*, **27**, 6158–6183.

51. Gordon-Soffer, R., Weiss, L.E., Eshel, R., Ferdman, B., Nehme, E., Bercovici, M., et al., (2020). Microscopic scan-free surface profiling over extended axial ranges by point-spread-function engineering. *Sci. Adv.*, **6**

52. Jungmann, R., Avendaño, M.S., Woehrstein, J.B., Dai, M., Shih, W.M., Yin, P., (2014). Multiplexed 3D cellular super-resolution imaging with DNA-PAINT and Exchange-PAINT. *Nat. Methods*, **11**, 313–318.

53. Schellenberger, P., Kaufmann, R., Siebert, C.A., Hagen, C., Wodrich, H., Grunewald, K., (2014). High-precision correlative fluorescence and electron cryo microscopy using two independent alignment markers. *Ultramicroscopy*, **143**, 41–51.

54. Schorb, M., Briggs, J.A., (2014). Correlated cryo-fluorescence and cryo-electron microscopy with high spatial precision and improved sensitivity. *Ultramicroscopy*, **143**, 24–32.

55. van Driel, L.F., Valentijn, J.A., Valentijn, K.M., Koning, R. I., Koster, A.J., (2009). Tools for correlative cryo-fluorescence microscopy and cryo-electron tomography applied to whole mitochondria in human endothelial cells. *Eur. J. Cell Biol.*, **88**, 669–684.

56. Hell, S.W., Sahl, S.J., Bates, M., Zhuang, X.W., Heintzmann, R., Booth, M.J., The, et al., (2015). super-resolution microscopy roadmap. *J. Phys. D Appl. Phys.*, **2015**, 48.

57. Wolff, G., Hagen, C., Grünewald, K., Kaufmann, R., (2016). Towards correlative super-resolution fluorescence and electron cryo-microscopy. *Biol. Cell*, **108**, 245–258.

58. Schorb, M., Gaechter, L., Avinoam, O., Sieckmann, F., Clarke, M., Bebeacua, C., et al., (2017). New hardware and workflows for semi-automated correlative cryo-fluorescence and cryo-electron microscopy/tomography. *J. Struct. Biol.*, **197**, 83–93.

59. Kaufmann, R., Hagen, C., Grünewald, K., (2014). Fluorescence cryo-microscopy: current challenges and prospects. *Curr. Opin. Chem. Biol.*, **20**, 86–91.

60. Kaufmann, R., Schellenberger, P., Seiradake, E., Dobbie, I.M., Jones, E.Y., Davis, I., et al., (2014). Super-resolution microscopy using standard fluorescent proteins in intact cells under cryo-conditions. *Nano Lett.*, **14**, 4171–4175.

61. Chang, Y.-W., Chen, S., Tocheva, E.I., Treuner-Lange, A., Löbach, S., Søgaard-Andersen, L., et al., (2014). Correlated cryogenic photoactivated localization microscopy and cryo-electron tomography. *Nat. Methods*, **11**, 737–739.

62. Liu, B., Xue, Y., Zhao, W., Chen, Y., Fan, C., Gu, L., et al., (2015). Three-dimensional super-resolution protein localization correlated with vitrified cellular context. *Sci. Rep.*, **5**, 13017.

63. Xu, X., Xue, Y., Tian, B., Feng, F., Gu, L., Li, W., et al., (2018). Ultra-stable super-resolution fluorescence cryo-microscopy for correlative light and electron cryo-microscopy. *Sci. China Life Sci.*, **61**, 1312–1319.

64. Tuijtel, M.W., Koster, A.J., Jakobs, S., Faas, F.G.A., Sharp, T.H., (2019). Correlative cryo super-resolution light and electron microscopy on mammalian cells using fluorescent proteins. *Sci. Rep.*, **9**, 1369.

65. Dahlberg, P.D., Saurabh, S., Sartor, A.M., Wang, J., Mitchell, P.G., Chiu, W., et al., (2020). Cryogenic single-

molecule fluorescence annotations for electron tomography reveal in situ organization of key proteins in Caulobacter. *Proc. Natl. Acad. Sci. U. S. A.*, **117**, 13937–13944.

66. Schermelleh, L., Ferrand, A., Huser, T., Eggeling, C., Sauer, M., Biehlmaier, O., et al., (2019). Super-resolution microscopy demystified. *Nat. Cell Biol.*, **21**, 72–84.

67. Moser, F., Prazak, V., Mordhorst, V., Andrade, D.M., Baker, L.A., Hagen, C., et al., (2019). Cryo-SOFI enabling low-dose super-resolution correlative light and electron cryo-microscopy. *Proc. Natl. Acad. Sci. U. S. A.*, **116**, 4804–4809.

68. Prazak, V., Grunewald, K., Kaufmann, R., (2021). Correlative super-resolution fluorescence and electron cryo-microscopy based on cryo-SOFI. *Methods Cell Biol.*, **162**, 253–271.

69. Phillips, M.A., Harkiolaki, M., Susano Pinto, D.M., Parton, R.M., Palanca, A., Garcia-Moreno, M., et al., (2020). CryoSIM: super-resolution 3D structured illumination cryogenic fluorescence microscopy for correlated ultrastructural imaging. *Optica.*, **7**, 802–812.

70. Le Gros, M.A., McDermott, G., Uchida, M., Knoechel, C. G., Larabell, C.A., (2009). High-aperture cryogenic light microscopy. *J. Microsc.*, **235**, 1–8.

71. Faoro, R., Bassu, M., Mejia, Y.X., Stephan, T., Dudani, N., Boeker, C., et al., (2018). Aberration-corrected cryoimmersion light microscopy. *Proc. Natl. Acad. Sci. U. S. A.*, **115**, 1204–1209.

72. Balzarotti, F., Eilers, Y., Gwosch, K.C., Gynna, A.H., Westphal, V., Stefani, F.D., et al., (2017). Nanometer resolution imaging and tracking of fluorescent molecules with minimal photon fluxes. *Science*, **355**, 606–612.

73. Gwosch, K.C., Pape, J.K., Balzarotti, F., Hoess, P., Ellenberg, J., Ries, J., et al., (2020). MINFLUX nanoscopy delivers 3D multicolor nanometer resolution in cells. *Nat. Methods.*, **17**, 217–224.

74. Rigort, A., Bäuerlein, F.J., Villa, E., Eibauer, M., Laugks, T., Baumeister, W., et al., (2012). Focused ion beam micromachining of eukaryotic cells for cryoelectron tomography. *Proc. Natl. Acad. Sci. U. S. A.*, **109**, 4449–4454.

75. Schaffer, M., Engel, B.D., Laugks, T., Mahamid, J., Plitzko, J.M., Baumeister, W., (2015). Cryo-focused ion beam sample preparation for imaging vitreous cells by cryo-electron tomography. *Bio-Protocol.*, **5**

76. Rigort, A., Bäuerlein, F.J.B., Leis, A., Gruska, M., Hoffmann, C., Laugks, T., et al., (2010). Micromachining tools and correlative approaches for cellular cryo-electron tomography. *J. Struct. Biol.*, **172**, 169–179.

77. Tacke, S., Erdmann, P., Wang, Z., Klumpe, S., Grange, M., Plitzko, J., et al., (2021). A streamlined workflow for automated cryo focused ion beam milling. *J. Struct. Biol.*, **107743**

78. Toro-Nahuelpan, M., Zagoriy, I., Senger, F., Blanchoin, L., Thery, M., Mahamid, J., (2020). Tailoring cryo-electron microscopy grids by photo-micropatterning for in-cell structural studies. *Nat. Methods.*, **17**, 50–54.

79. Engel, L., Gaietta, G., Dow, L.P., Swif, M.F., Pardon, G., Volkmann, N., et al., (2019). Extracellular matrix micropatterning technology for whole cell cryogenic electron microscopy studies. *J. Micromech. Microeng.*, **29**, 115018

80. Zachs, T., Schertel, A., Medeiros, J., Weiss, G.L., Hugener, J., Matos, J., et al., (2020). Fully automated, sequential focused ion beam milling for cryo-electron tomography. *Elife.*, **9**

81. Buckley, G., Gervinskas, G., Taveneau, C., Venugopal, H., Whisstock, J.C., de Marco, A., (2020). Automated cryo-lamella preparation for high-throughput in-situ structural biology. *J. Struct. Biol.*, **210**, 107488

82. Klumpe, S., Fung, H.K.H., Goetz, S.K., Zagoriy, I., Hampoelz, B., Zhang, X., et al., (2021). A modular platform for streamlining automated cryo-FIB workflows. *bioRxiv*,. https://doi.org/10.1101/2021.05.19.444745.

83. Gorelick, S., Korneev, D., Handley, A., Gervinskas, G., Oorschot, V., et al., (2018). Oxygen plasma focused ion beam scanning electron microscopy for biological samples. *bioRxiv*,. https://doi.org/10.1101/457820.

84. Fu, X., Ning, J., Zhong, Z., Ambrose, Z., Charles Watkins, S., Zhang, P., (2019). AutoCLEM: An automated workflow for correlative live-cell fluorescence microscopy and cryo-electron tomography. *Sci. Rep.*, **9**, 19207.

85. Mastronarde, D.N., (2005). Automated electron microscope tomography using robust prediction of specimen movements. *J. Struct. Biol.*, **152**, 36–51.

86. D.R. Morado, B. Hu, J. Liu, Using tomoauto: a protocol for high-throughput automated cryo-electron tomography, J. Vis. Exp. 2016:e53608.

87. Brönnimann, C., Eikenberry, E.F., Horisberger, R., Hülsen, G., Schmitt, B., Schulze-Briese, C., et al., (2003). Continuous sample rotation data collection for protein crystallography with the PILATUS detector. *Nucl. Instrum. Methods Phys. Res., Sect. A*, **510**, 24–28.

88. Chreifi, G., Chen, S., Metskas, L.A., Kaplan, M., Jensen, G.J., (2019). Rapid tilt-series acquisition for electron cryotomography. *J. Struct. Biol.*, **205**, 163–169.

89. Karuppasamy, M., Karimi Nejadasl, F., Vulovic, M., Koster, A.J., Ravelli, R.B.G., (2011). Radiation damage in single-particle cryo-electron microscopy: effects of dose and dose rate. *J. Synchrotron Radiation*, **18**, 398–412.

90. Grant, T., Grigorieff, N., (2015). Measuring the optimal exposure for single particle cryo-EM using a 2.6 Å reconstruction of rotavirus VP6. *eLife*, **4**, e06980

91. Glaeser, R.M., (2016). Chapter two - Specimen behavior in the electron beam. In: Crowther, R.A. (Ed.)*, Methods in Enzymology*,. Academic Press, pp. 19–50.

92. Hagen, W.J.H., Wan, W., Briggs, J.A.G., (2017). Implementation of a cryo-electron tomography tilt-scheme optimized for high resolution subtomogram averaging. *J. Struct. Biol.*, **197**, 191–198.

93. Turonova, B., Hagen, W.J.H., Obr, M., Mosalaganti, S., Beugelink, J.W., Zimmerli, C.E., et al., (2020). Benchmarking tomographic acquisition schemes for high-resolution structural biology. *Nat. Commun.*, **11**, 876.

94. Langmore, J.P., Smith, M.F., (1992). Quantitative energy-filtered electron microscopy of biological molecules in ice. *Ultramicroscopy*, **46**, 349–373.

95. Danev, R., Buijsse, B., Khoshouei, M., Plitzko, J.M., Baumeister, W., (2014). Volta potential phase plate for in-focus phase contrast transmission electron microscopy. *Proc. Natl. Acad. Sci.*, **111**, 15635–15640.

96. Danev, R., Baumeister, W., (2017). Expanding the boundaries of cryo-EM with phase plates. *Curr. Opin. Struct. Biol.*, **46**, 87–94.

97. Buijsse, B., Trompenaars, P., Altin, V., Danev, R., Glaeser, R.M., (2020). Spectral DQE of the volta phase plate. *Ultramicroscopy*, **218**, 113079

98. Asano, S., Fukuda, Y., Beck, F., Aufderheide, A., Förster, F., Danev, R., et al., (2015). A molecular census of 26S proteasomes in intact neurons. *Science*, **347**, 439–442.

99. Imhof, S., Zhang, J., Wang, H., Bui, K.H., Nguyen, H., Atanasov, I., et al., (2019). Cryo electron tomography with volta phase plate reveals novel structural foundations of the 96-nm axonemal repeat in the pathogen Trypanosoma brucei. *Elife*, **8**

100. Schwartz, O., Axelrod, J.J., Campbell, S.L., Turnbaugh, C., Glaeser, R.M., Muller, H., (2019). Laser phase plate for transmission electron microscopy. *Nat. Methods*, **16**, 1016–1020.

101. Frangakis, A.S., Hegerl, R., (2001). Noise reduction in electron tomographic reconstructions using nonlinear anisotropic diffusion. *J. Struct. Biol.*, **135**, 239–250.

102. Rigort, A., Günther, D., Hegerl, R., Baum, D., Weber, B., Prohaska, S., et al., (2012). Automated segmentation of electron tomograms for a quantitative description of actin filament networks. *J. Struct. Biol.*, **177**, 135–144.

103. Tegunov, D., Cramer, P., (2019). Real-time cryo-electron microscopy data preprocessing with Warp. *Nat. Methods*, **16**, 1146–1152.

104. Weigert, M., Schmidt, U., Boothe, T., Müller, A., Dibrov, A., Jain, A., et al., (2018). Content-aware image restoration: pushing the limits of fluorescence microscopy. *Nat. Methods*, **15**, 1090–1097.

105. Buchholz, T., Jordan, M., Pigino, G., Cryo-CARE, Jug F., (2019). Content-aware image restoration for cryo-transmission electron microscopy data. *I S Biomed. Imaging*,, 502–506.

106. Bepler, T., Kelley, K., Noble, A.J., Berger, B., (2020). Topaz-Denoise: general deep denoising models for cryoEM and cryoET. *Nat. Commun.*, **11**, 5208.

107. Lehtinen, J., Munkberg, J., Hasselgren, J., Laine, S., Karras, T., Aittala, M., et al., (2018). Noise2Noise: Learning image restoration without clean data. In: Jennifer, D., Andreas, K. (Eds.), *Proceedings of the 35th International Conference on Machine Learning. Proceedings of Machine Learning Research: PMLR*,, pp. 2965–2974.

108. Li, X., Mooney, P., Zheng, S., Booth, C.R., Braunfeld, M. B., Gubbens, S., et al., (2013). Electron counting and beam-induced motion correction enable near-atomic-resolution single-particle cryo-EM. *Nat. Methods*, **10**, 584–590.

109. Zheng, S.Q., Palovcak, E., Armache, J.-P., Verba, K.A., Cheng, Y., Agard, D.A., (2017). MotionCor2: anisotropic correction of beam-induced motion for improved cryo-electron microscopy. *Nat. Methods*, **14**, 331–332.

110. Brilot, A.F., Chen, J.Z., Cheng, A., Pan, J., Harrison, S.C., Potter, C.S., et al., (2012). Beam-induced motion of vitrified specimen on holey carbon film. *J. Struct. Biol.*, **177**, 630–637.

111. Fernandez, J.-J., Li, S., Bharat, T.A.M., Agard, D.A., (2018). Cryo-tomography tilt-series alignment with consideration of the beam-induced sample motion. *J. Struct. Biol.*, **202**, 200–209.

112. Fernandez, J.-J., Li, S., Agard, D.A., (2019). Consideration of sample motion in cryo-tomography based on alignment residual interpolation. *J. Struct. Biol.*,.

113. Himes, B.A., Zhang, P., (2018). emClarity: software for high-resolution cryo-electron tomography and subtomogram averaging. *Nat. Methods*, **15**, 955–961.

114. Chen, M., Bell, J.M., Shi, X., Sun, S.Y., Wang, Z., Ludtke, S.J., (2019). A complete data processing workflow for cryo-ET and subtomogram averaging. *Nat. Methods*, **16**, 1161–1168.

115. Grant, T., Rohou, A., Grigorieff, N., (2018). cisTEM, user-friendly software for single-particle image processing. *Elife*, **7**

116. Zivanov, J., Nakane, T., Forsberg, B.O., Kimanius, D., Hagen, W.J., Lindahl, E., et al., (2018). New tools for automated high-resolution cryo-EM structure determination in RELION-3. *Elife*, **7**

117. Honari, S., Molchanov, P., Tyree, S., Vincent, P., Pal, C., Kautz, J., (2018). Improving landmark localization with semi-supervised learning. *In: 2018 IEEE/CVF Conference on Computer Vision and Pattern Recognition*,, pp. 1546–1555.

118. Jasnin, M., Ecke, M., Baumeister, W., Gerisch, G., (2016). Actin organization in cells responding to a perforated surface, revealed by live imaging and cryo-electron tomography. *Structure*, **24**, 1031–1043.

119. Tao, C.L., Liu, Y.T., Sun, R., Zhang, B., Qi, L., Shivakoti, S., et al., (2018). Differentiation and characterization of excitatory and inhibitory synapses by cryo-electron tomography and correlative microscopy. *J. Neurosci.*, **38**, 1493–1510.

120. Blum, T.B., Hahn, A., Meier, T., Davies, K.M., Kuhlbrandt, W., (2019). Dimers of mitochondrial ATP synthase induce membrane curvature and self-assemble into rows. *Proc. Natl. Acad. Sci. U. S. A.*, **116**, 4250–4255.

121. Martins, B., Sorrentino, S., Chung, W.-L., Tatli, M., Medalia, O., Eibauer, M., (2021). Unveiling the polarity of actin filaments by cryo-electron tomography. *Structure*, **29**, 488–984.

122. Chaikeeratisak, V., Nguyen, K.T., Khanna, K., Brilot, A.F., Erb, M., Coker, J., et al., (2017). Assembly of a nucleus-like structure during viral replication in bacteria. *Science*, **355**, 194–197.

123. Martinez-Sanchez, A., Garcia, I., Asano, S., Lucic, V., Fernandez, J.-J., (2014). Robust membrane detection based on tensor voting for electron tomography. *J. Struct. Biol.*, **186**, 49–61.

124. Rusu, M., Starosolski, Z., Wahle, M., Rigort, A., Wriggers, W., (2012). Automated tracing of filaments in 3D electron tomography reconstructions using Sculptor and Situs. *J. Struct. Biol.*, **178**, 121–128.

125. Böhm, J., Frangakis, A.S., Hegerl, R., Nickell, S., Typke, D., Baumeister, W., (2000). Toward detecting and identifying macromolecules in a cellular context: Template matching applied to electron tomograms. *Proc. Natl. Acad. Sci.*, **97**, 14245–14250.

126. Winkler, H., (2007). 3D reconstruction and processing of volumetric data in cryo-electron tomography. *J. Struct. Biol.*, **157**, 126–137.

127. Heumann, J.M., Hoenger, A., Mastronarde, D.N., (2011). Clustering and variance maps for cryo-electron tomography using wedge-masked differences. *J. Struct. Biol.*, **175**, 288–299.

128. Hrabe, T., Chen, Y., Pfeffer, S., Kuhn Cuellar, L., Mangold, A.-V., Förster, F., (2012). PyTom: A python-based toolbox for localization of macromolecules in cryo-electron tomograms and subtomogram analysis. *J. Struct. Biol.*, **178**, 177–188.

129. Galaz-Montoya, J.G., Flanagan, J., Schmid, M.F., Ludtke, S.J., (2015). Single particle tomography in EMAN2. *J. Struct. Biol.*, **190**, 279–290.

130. Bharat, T.A., Scheres, S.H., (2016). Resolving macromolecular structures from electron cryo-tomography data using subtomogram averaging in RELION. *Nat. Protoc.*, **11**, 2054–2065.

131. Castano-Diez, D., (2017). The Dynamo package for tomography and subtomogram averaging: components for MATLAB, GPU computing and EC2 Amazon Web Services. *Acta Crystallogr. D Struct.. Biol.*, **73**, 478–487.

132. Wan, W., Khavnekar, S., Wagner, J., Erdmann, P., Baumeister, W., (2020). STOPGAP: A software package for subtomogram averaging and refinement. *Microsc. Microanal.*, **26** (S2), 2516.

133. Rickgauer, J.P., Grigorieff, N., Denk, W., (2017). Single-protein detection in crowded molecular environments in cryo-EM images. *Elife*, **6**

134. Lucas, B.A., Himes, B.A., Xue, L., Grant, T., Mahamid, J., Grigorieff, N., (2021). Locating macromolecular assemblies in cells by 2D template matching with cisTEM. *Elife*, **10**

135. Martinez-Sanchez, A., Kochovski, Z., Laugks, U., Meyer Zum Alten Borgloh, J., Chakraborty, S., Pfeffer, S., et al., (2020). Template-free detection and classification of membrane-bound complexes in cryo-electron tomograms. *Nat. Methods*, **17**, 209–216.

136. Moebel, E., Martinez-Sanchez, A., Lamm, L., Righetto, R., Wietrzynski, W., Albert, S., et al., (2021). Deep learning improves macromolecule identification in 3D cellular cryo-electron tomograms. *bioRxiv,*. https://doi.org/10.1101/2020.04.15.042747.

137. Zeng, X., Kahng, A., Xue, L., Mahamid, J., Chang, Y.-W., Xu, M., (2021). DISCA: high-throughput cryo-ET structural pattern mining by deep unsupervised clustering. *bioRxiv,*. https://doi.org/10.1101/2021.05.16.444381.

138. Tagari, M., Newman, R., Chagoyen, M., Carazo, J.M., Henrick, K., (2002). New electron microscopy database and deposition system. *Trends Biochem. Sci.*, **27**, 589.

139. Iudin, A., Korir, P.K., Salavert-Torres, J., Kleywegt, G.J., Patwardhan, A., (2016). EMPIAR: a public archive for raw electron microscopy image data. *Nat. Methods*, **13**, 387–388.

140. Ortega, D.R., Oikonomou, C.M., Ding, H.J., Rees-Lee, P., Alexandria, , Jensen, G.J., (2019). ETDB-Caltech: A blockchain-based distributed public database for electron tomography. *PLoS One*, **14** e0215531.